Evaluation of SMAP, SMOS, and AMSR2 soil moisture products based on distributed ground observation network in cold and arid regions of China

Zengyan Wang, Tao Che, Tianjie Zhao, Liyun Dai, Xiaojun Li, Jean-Pierre Wigneron

Evaluation of SMAP, SMOS, and AMSR2 Soil Moisture Products Based on Distributed Ground Observation Network in Cold and Arid Regions of China

Zengyan Wang, Tao Che ⓘ, *Member, IEEE*, Tianjie Zhao ⓘ, *Senior Member, IEEE*, Liyun Dai ⓘ, Xiaojun Li ⓘ, and Jean-Pierre Wigneron, *Senior Member, IEEE*

Abstract—Long-term surface soil moisture (SM) data are increasingly needed in water budget and energy balance analysis of watersheds. The performance of nine remotely sensed SM products from Advanced Microwave Scanning Radiometer 2 (AMSR2), Soil Moisture and Ocean Salinity (SMOS), and Soil Moisture Active Passive (SMAP) missions are evaluated based on observations collected from distributed observation networks in the Heihe River Basin (HRB) of China during 2013 to 2017. Results show that the SMAP Level 3 dual channel algorithm SM retrievals reflect the seasonal SM variations well with high temporal correlations of ∼0.7 and high accuracy within 0.04 m³/m³ in terms of unbiased root mean squared error (ubRMSE) over the grassland in the HRB. The SMOS level 3 SM retrievals present increased underestimation and ubRMSE of ∼0.10 m³/m³ as the vegetation increases. The newly published SMOS Institut National de la Recherche Agronomique–Centre d'Etudes Spatiales de la BIOsphère product in version 2 outperforms the SMOS level 3 product with improved temporal correlation coefficient above 0.4 and lower ubRMSE of ∼0.05 m³/m³. AMSR2 Land Parameter Retrieval Algorithm SM products show extremely large overestimation over the vegetated regions in HRB, especially the C-band products. Drastically high underestimation biases are observed in the Japan Aerospace Exploration Agency AMSR2 SM product. Parameter uncertainty analyses indicate that the different parameterization schemes of vegetation optical depth inputs could be one of the main reasons resulting in the systematic overestimation/underestimation biases in the AMSR2/SMOS/SMAP SM retrievals. The findings aim to provide insights into studies on algorithms refinements and data fusions of SM products in HRB.

Index Terms—Evaluation, Heihe River Basin (HRB), Japan Aerospace Exploration Agency (JAXA), Land Parameter Retrieval Algorithm (LPRM), Soil Moisture Active Passive (SMAP), Soil Moisture and Ocean Salinity (SMOS)-IC, Soil Moisture (SM).

I. INTRODUCTION

SURFACE soil moisture (SM) is a key variable in land–atmosphere interactions affecting the land surface energy, water budget, and the carbon cycle at a global, regional, and watershed scale. Long-term and large-scale surface SM datasets are widely used in diverse fields of water resource management [1], food security [2], and extreme weather events (drought, flood, heatwave, etc.) predictions [3], [4], and so on. Passive microwave remote sensing has been increasingly recognized as the most effective way in SM monitoring, owing to the its unique, strong relationship with the soil dielectric properties, as well as its good temporal resolutions of 2–3 days. The currently operated passive microwave satellites/sensors provide continuously updated observations at various spatial and temporal resolutions. The Advanced Microwave Scanning Radiometer 2 (AMSR2) onboard the Global Change Observation Mission-Water (GCOM-W1) satellite launched in 2012 [5], is the successor of AMSR-E which enable the distribution of the first global standard SM products with the resolution of 25 km at both C- and X-band [6]. Other two SM monitoring satellites include the Soil Moisture and Ocean Salinity (SMOS) and the Soil Moisture Active Passive (SMAP), which were successively launched in 2009 and 2015, respectively. Both of them are expected to achieve more accurate SM products due to the higher capability of L-band in penetrating vegetation and soil compared to the C- or X-band technologies [7], [8].

Theoretically, the passive microwave remotely sensed SM products are retrieved through the combination of a radiative

Zengyan Wang is with the Key Laboratory of Geospatial Technology for the Middle and Lower Yellow River Regions, Henan University, Ministry of Education, Kaifeng 475004, China and also with the College of Geography and Environmental Science, Henan University, Kaifeng 475004, China (e-mail: wangzengyan@henu.edu.cn).

Tao Che is with the Heihe Remote Sensing Experimental Research Station, Key Laboratory of Remote Sensing of Gansu Province, Northwest Institute of Eco-Environment and Resources, Chinese Academy of Sciences, Lanzhou 730000, China and also with the Center for Excellence in Tibetan Plateau Earth Sciences, Chinese Academy of Sciences, Beijing 100101, China (e-mail: chetao@lzb.ac.cn).

Tianjie Zhao is with the State Key Laboratory of Remote Sensing Science, Aerospace Information Research Institute, Chinese Academy of Sciences, Beijing 100101, China (e-mail: zhaotj@aircas.ac.cn).

Liyun Dai is with the Heihe Remote Sensing Experimental Research Station, Key Laboratory of Remote Sensing of Gansu Province, Northwest Institute of Eco-Environment and Resources, Chinese Academy of Sciences, Lanzhou 730000, China (e-mail: dailiyun@lzb.ac.cn).

Xiaojun Li and Jean-Pierre Wigneron are with the Interactions Sol Plante Atmosphere, INRAE Bordeaux, 33140 Villenave-d'Ornon, France (e-mail: xiaojun.li@inra.fr; jean-pierre.wigneron@inra.fr).

Digital Object Identifier 10.1109/JSTARS.2021.3108432

transfer model together with a semi-empirical soil dielectric model. Operational SM retrieval algorithms and products are provided by different research groups throughout the world. To date, the most successfully applied SM algorithms include the single channel algorithm (SCA) and dual channel algorithm (DCA) as the baseline/optional retrieval algorithms for the SMAP mission [9], the 2-Parameter inversion of the L-band Microwave Emission of the Biosphere (L-MEB) model for SMOS with multiangular capabilities [10]–[12], the look-up table algorithm developed by the Japan Aerospace Exploration Agency (JAXA) for AMSR2 [13], [14], and the Land Parameter Retrieval Algorithm (LPRM) provided by the groups of VU University Amsterdam for both C-, X-, and L-band observations of AMSR2, SMOS, and SMAP likewise [15]. However, the algorithms are experiencing continuous improvement with new calibrations and parameter optimizations in their development [16]–[18], and new versions of SM products are consistently updated nowadays. For one example, an alternative SMOS Institut National de la Recherche Agronomique (INRA)–Centre d'Etudes Spatiales de la BIOsphère (CESBIO) (SMOS-IC) SM product in version 105 was developed by the INRA and CESBIO in 2017 relying on a simplified but improved SM retrieval algorithm initially proposed for the SMOS official products. More recently, the upgraded SMOS-IC product in version 2 was published in 2020, which encouraged more evaluations and discussions in applications [19].

The evaluation/validation of the existing SM products is critical for better understanding their error characteristics and for their further refinement and applications. Direct validations through comparisons with ground SM observations are gaining prevalence as dense SM observation/validation networks are established over various land cover types and in different climate zones through the world [20]–[24]. In China, long-term evaluation of satellite SM products were mainly conducted over the alpine meadow in the cold semiarid regions of Qinghai-Tibet Plateau [25]–[27], relying on the multiscale SM and soil temperature monitoring networks, such as Tibet-Obs and Soil Moisture and Temperature Monitoring Network on the central TP since 2002 [28], [29]. In recent years, new SM experiments are conducted outside Tibetan plateau on the scale of watershed in support of the hydrological cycle studies [30], [31]. Currently, the evaluation and comparison works are still focused on the scale of watershed in China [16], [32]. One distributed ecohydrological ground observation network in the semiarid regions of northwest China were established during the field campaigns in the Heihe Watershed allied Telmetry Experimental Research (HiWATER) since 2012 [33]. The accumulated and abundant ground observations collected in the Heihe River Basin (HRB) make it a promising testbed for remote sensing products evaluation, algorithms development, and researches on the scaling, heterogeneity, and the uncertainty problems as well.

This research aims to provide a comprehensive evaluation of nine passive microwave remotely sensed SM products over the diverse land cover and land surface conditions in HRB, and the error source analyses are also conducted from the perspective of parameterization in SM retrieval algorithms to provide new insights into the various performances of these SM products

and to help obtaining long-term and highly accurate datasets for regional hydrological and climatic studies in future. The satellite-based SM products to be evaluated include four AMSR2 SM products, two SMOS SM products, and three SMAP SM products form different SM retrieval algorithms. The article is organized as follows. The datasets and metrics are briefly introduced in Section II. Evaluation results are presented in Section III, and the error source analyses from the perspective of algorithm parameterization are discussed in Section IV. Conclusions are summarized in Section V.

II. MATERIAL AND METHODS

A. Study Area

The HRB (37.5°N–43°N, 97°E–102°E, Fig. 1), located in the semiarid regions of Northwest China, is the second largest inner river basin in China. The area is with complex terrain. The elevations gradually decrease from about 3200 to 850 m from up to downstream HRB. The region is characterized by its distinct cold and arid climates. The annual precipitation gradually decreases from around 350 to below 50 mm, and the annual potential evaporation increase from around 1000 to above 2000 mm from up to downstream HRB, resulting in totally different landscapes and SM conditions. In the upstream area, typical cold region species of alpine grassland, swamp, alpine meadow, valley bush, Qilian juniper, and others compose the main landscapes. Permafrost, seasonal frozen soil, alpine cold desert, snow, and glaciers coexist in the area. The midstream region is featured as the artificial oasis–riparian ecosystem–wetland–desert compound, and the major landscapes are maize crops, steppes and Gobi desert. The downstream region is a typical arid natural oasis with sparse vegetation and sandy/gravel deserts. Populus euphratica, Tamarix, and other arid region species are sparsely distributed near the river bank, forming the main landscapes.

B. Ground Observation Networks

As shown in Fig. 1, three nested SM observation networks are established throughout HRB during the HiWATER field campaigns [33], namely the hydrometeorological network composed of 18 automatic weather stations (AWS) over the whole basin, the ecohydrological wireless sensor networks with 40 SM soil temperature sites(SMSTS)located in the Babao sub-basin in the upstream HRB (SMSTS-UP), and the ecohydrological wireless sensor networks with 9 SMSTS equipped in the 5 × 5 km corn field in the artificial oasis of midstream HRB (SMSTS-MID). Layered SM and soil temperature (Ts, K) observations at multiple depth of 4, 10, 20, 40, 80, 120, and 160 cm are simultaneously measured by CS616 (Campbell Scientific, USA) sensors and SI-111 infrared radiometer every 10 min in each AWS node. The SMSTS-UP and SMSTS-MID nodes provide SM and soil temperature observations every 1 h for three layers of 4, 10, and 20 cm below surface. The SM is measured by a Steven Hydro Probe II sensor based on the frequency-domain reflectometry method in each SMSTS node. Field calibration of the instruments is conducted through comparisons against
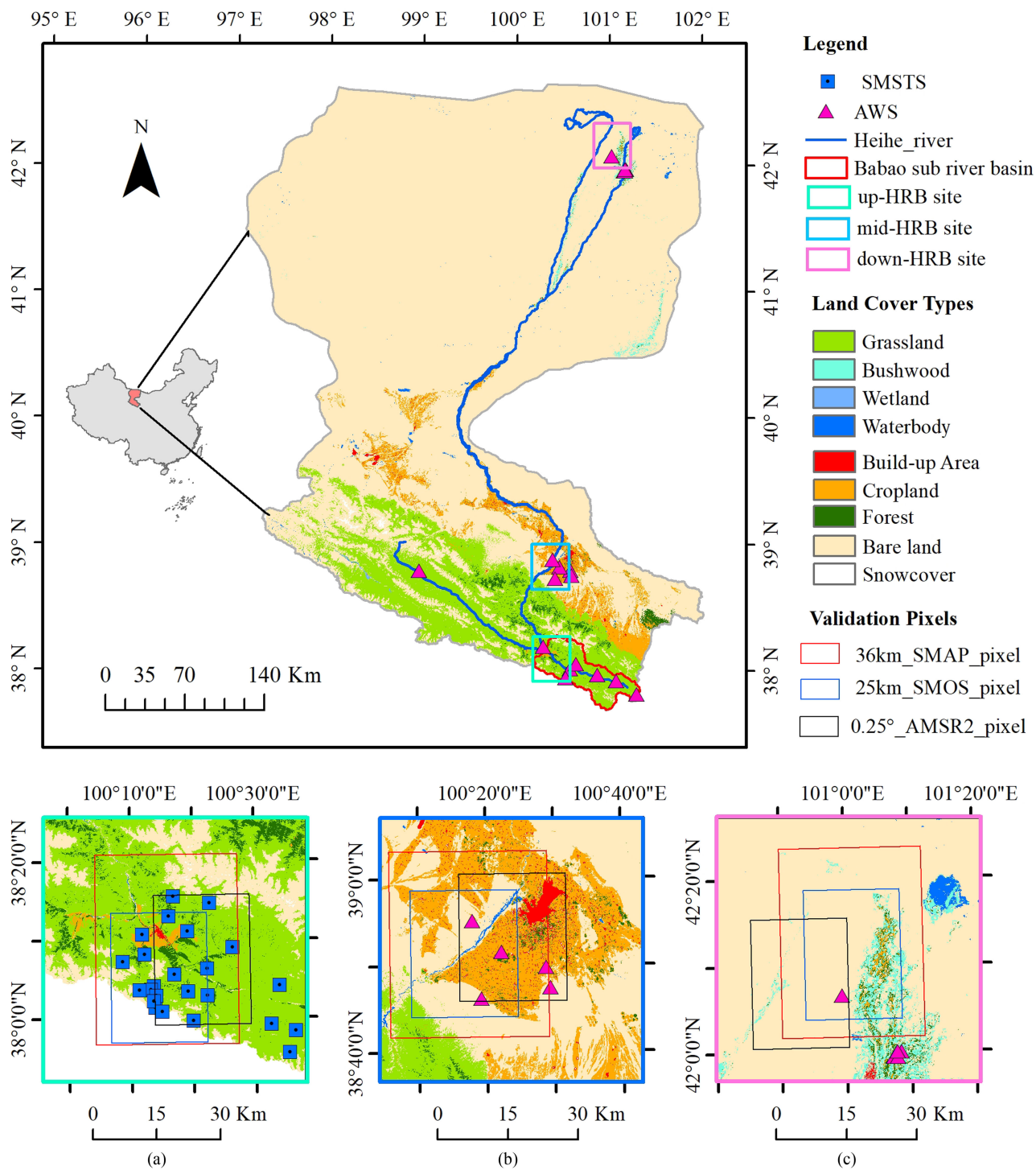
Fig. 1. Land cover types and the distributed soil moisture observation networks in three evaluation sites of up-HRB (a), mid-HRB (b), and down-HRB (c) in HRB.

the gravimetric method before their installation [34]. The systematic errors are linearly removed before their applications. The accuracy of the CS616 and Hydro Probe II instruments are calibrated to be 0.025 and 0.011 m³/m³, respectively. The accuracy of the surface radiative temperature for SI-111 is 0.15 °C.

Three evaluation sites at the 30 km averaged satellite resolution are selected in the up-, mid-, and down-HRB, respectively. The variant numbers of observation nodes, distinct heterogeneous land cover types, and surface terrain conditions for each site are summarized in Table I. The site averaged SM and Ts measurements at 0–5, 20–40 cm depth as well as the daily

TABLE I
BASIC INFORMATION ABOUT THE THREE EVALUATION SITES IN HRB

Evaluation sites	Main Land cover types (%)	Mean Elevation and the Root Mean Error, m	Number of observation nodes in each evaluation site
Up-HRB	Alpine meadow, 80%; Forest, 9%	3442.1 (440.4)	1AWS+8 SMSTS
Mid-HRB	Cropland, 42%; desert, 43%	1556 (67.4)	4 AWS+9 SMSTS
Down-HRB	Desert, 85%; Bush wood, 8%	922.2 (11.1)	1 AWS

TABLE II
BASIC INFORMATION ABOUT THE NINE SATELLITE-BASED SM PRODUCTS

SM Datasets	JAXA- X	LPRM- C1	LPRM- C2	LPRM-X	SMOS-L3	SMOS-IC	SMAP-SCAH	SMAP-SCAV	SMAP-DCA
Satellite Platform		AMSR2				SMOS		SMAP	
Incidence Angle		55°				0-55°		40°	
Frequency (GHz)	10.7	6.9	7.3	10.7		1.4		1.41	
Ascending time		13:30				6:00		18:00	
Descending time		1:30				18:00		6:00	
Spatial Resolution		0.25°				25km		43km	

precipitation data from 2013 to 2017 during the HiWATER experiment are extracted from the networks to conduct evaluation and error analyses of the seven SM products in this study. All the AWS and SMSTS data are freely provided by the National Tibetan Plateau Data Center[1] [35], [36]. The fine resolution (30 m) land cover map in Fig. 1 is mapping based on the time series HJ-1/CCD data in 2012, which is also downloaded from[2] [37]. Other complementary information about vegetation and land surface conditions include the MODIS NDVI dataset in MOD13A1 at the temporal resolution of 16 days and spatial resolution of 500 m in Equal-Area Scalable Earth Grid (EASE) grid projection from the earth data portal of[3] and the global 1 km digital elevation model of GTOPO30 on the USGS website of[4].

C. Satellite-Based Soil Moisture Products

In this article, nine satellite SM products retrieved from SMOS, SMAP, and AMSR2 at both ascending and descending orbits during the HiWATER field campaign from 2013 to 2017 are collected. Basic information about the datasets are summarized in Table II, and the detailed parameterization schemes in the retrieval algorithms are compared in Table III.

1) SMAP SM Product: SMAP is a NASA satellite mission launched in 2015 to monitor the global SM and landscape freeze/thaw state [8]. The satellite is carrying an L-band radar

(1.26 GHz, ceasing operation after about three months of working) and an L-band radiometer (1.41 GHz, operational) to provide observations on a fixed (40°) incidence angle with a wide (1000 km) swath width. The project is designed to provide global SM estimations in the top 5 cm of soil with an accuracy within 0.04 cm³/cm³ at around 40 km spatial resolution and 3-day average temporal intervals.

Daily grid composites of the SMAP passive level-3 product (L3_SM_P, version 007) is evaluated in this article. The SMAP L3_SM_P product implements three operational SM retrieval algorithms to achieve the SM datasets, namely the SCA at V polarization (baseline), SCA at H polarization (optional), and DCA (optional). In this article, all the three SMAP level 3 SM products of SMAP-SCAH/SCAV and SMAP-DCA are all discussed in comparison with the SM retrievals from both SMOS and AMSR2 products. The datasets are freely available from the National Snow and Ice Data Center.[5] All the products are provided at a fixed resolution of 36 km in EASE-grid 2.0 projection. Due to the late launch of SMAP satellite, a short period of SMAP L3_SM_P product for three years from 2015 to 2017 is used.

In the SMAP algorithms, the SM retrievals are related to soil emissivity through the Mironov dielectric mixing model and semi-empirical surface roughness Q-H model to correct the surface roughness effects. The emission of the soil is simulated by the emissivity and physical temperature of the emitting soil layer (Te, K). The attenuation effect of the overlying vegetation on the emitted energy from soil is modeled as a function of the

[1][Online]. Available: https://data.tpdc.ac.cn
[2][Online]. Available: https://data.tpdc.ac.cn
[3][Online]. Available: https://search.earthdata.nasa.gov/search
[4][Online]. Available: https://earthexplorer.usgs.gov/

[5][Online]. Available: https://nsidc.org/data/SPL3FTP/versions/2

TABLE III
MAIN COMPONENTS IN THE OPERATIONAL SM RETRIEVAL ALGORITHMS OF THE NINE SATELLITE-BASED SM DATASETS

SM Datasets	JAXA-X	LPRM-C1, C2, X	SMOS-L3	SMOS- IC	SMAP SCAH, SCAV	SMAP-DCA
Algorithm	LUT	LPRM	Multi-orbit SMOS L2 SM processor	2-P retrieval algorithm based on L-MEB	SCAH, SCAV	DCA
Frequency (GHz)	10.65, 36.5	6.9/7.3/10.65, 36.5	1.4	1.4	1.41	1.41
Soil temperature of the emitting layer (Te)	Te=293 K	Te =0.688TB_V$_{36.5}$ $_{GHz}$+101.126	Te= f(Ts_deep, Ts_surf), where Ts_deep and Ts_surf are from ECMWF	Te= f(Ts_deep, Ts_surf), where Ts_deep and Ts_surf are from ECMWF	Te = f(Ts_deep, Ts_surf), where Ts_deep and Ts_surf are form GEOS-5	Te = f(Ts_deep, Ts_surf), where Ts_deep and Ts_surf are form GEOS-5
Vegetation temperature (Tv)	Tv= Te	Tv= Te	Tv= Te	Tv= ECMWF Tskin	Tv= Te	Tv= Te
Vegetation Optical depth (VOD)	VOD=b*VWC; b is constants; VWC is retrieved using lookup table;	VOD=f (MPDI, k,θ, ω); MDPI=(TBV-TBH)/(TBV+TBH)	VOD is simultaneously retrieved with SM in the 2P L-MEB algorithm	VOD is simultaneously retrieved with SM in the 2P L-MEB algorithm	VOD =b*VWC; b=f(IGBP); VWC=f(NDVI, IGBP), NDVI from MODIS	VOD is simultaneously retrieved with SM in the DCA algorithm
Albedo (ω)	Constant ω, ω$_H$= 0.061 and ω$_V$ = 0.063 for X-band;	ω=0.06	ω=0.06-0.08 for forest, and ω=0 for other low vegetation canopies;	ω=f(IGBP), Constant ω between 0.08 to 0.12	Constant ω=f(IGBP), varying from 0.03 to 0.08	ω=f(IGBP), Constant ω between 0.05 to 0.07
Soil roughness model	Q/H model, with Q=0.189 and H$_R$= 0.873 for X-band;	Q/H model, with constant Q=0.2 and H$_R$=0.2	Q/H model, with Q=0, N$_{RH}$ =2, N$_{RV}$ =0, H$_R$ =0.3 for forests, and H$_R$ =0.1 for other types;	Q/H model, with Q=0, N$_R$ = -1, and H$_R$ = f(IGBP) varying from 0.02 to 0.47	Q/H model, with Q= 0.1771 H$_R$, N$_H$ = N$_V$=2, and constant H$_R$ = f(IGBP) varying from 0.083 to 0.16	Q/H model, with Q= 0.1771 H$_R$, N$_H$ = N$_V$=2, and constant H$_R$ = f(IGBP) varying from 0.083 to 0.16
Soil dielectric model	Dobson et al., 1985	Wang & Schmugge, 1981	Dobson et al., 1985	Mironov et al., 2009	Mironov et al., 2009	Mironov et al., 2009

vegetation optical depth (VOD), which could be calibrated based on the vegetation water content (VWC, kg/m^2) observations through an empirical relationship of VOD = b ∗ VWC, where the empirical b factor is changing depending on the vegetation structure, polarization, and frequency. The emission ability of the vegetation is simulated by a simplified parameter of single scattering albedo (ω), which tends to be very small at L-band and set to be nonzero in the SMAP algorithms. In the inversion process, important model inputs including Te, surface roughness (H$_R$), and polarization mixing factor (Q) in the Q-H model, vegetation parameters of ω, and VOD in the radiative transfer model, are provided based on the ancillary datasets, which has been summarized in Table III. The SMAP SM retrieval algorithms obtain the surface SM simulations (and VOD in the SMAP-DCA product) by minimizing the cost function between the modeled and observed TB values on either horizontal, vertical, or both polarizations. More details about the algorithm can be found in [38].

In the article, the recommended data flittering of "retrieval qual flag" value to be 0 or 8 is adopted to keep the high-quality retrievals to be analyzed in the SMAP SM data preprocessing. The filtered unsatisfied retrievals are mostly labeled as Mountainous Terrain (slope standard deviation > 3°), frozen soil (frozen soil fraction > 0.05), and surface covered with snow (snow fraction > 0.05) in the HRB.

2) SMOS SM Products: The SMOS mission, developed by ESA with contributions from Centre National d'Etudes Spatiales and Centro para el Desarrollo Tecnológico Industrial, was launched in 2009. It is the first satellite carrying the L-band (1.4 GHz) radiometer to provide global SM and ocean salinity datasets from space [7]. The satellite runs in a sunsynchronous orbit at the ascending/descending overpass time of 6:00 A.M./6:00 P.M., respectively. The unique capability of the SMOS instrument is to obtain the dual polarized brightness temperature (TB) observations over a wide range of incidence angles (∼0–60°), with the spatial resolution of ∼43 km and 3-day revisit. The multiangular viewing capability of SMOS instrument enable the simultaneous retrieval of SM and VOD. Three grid composites (level 3) of global SMOS SM datasets are currently available, namely the SMOS Level 3 CADTS SM product (hereinafter referred to as SMOS-L3 for simplicity), the SMOS Level 3 BEC (SMOS-BEC) SM product, and the SMOS Level 3 INRA-CESBIO (SMOS-IC) SM product. Among them, the SMOS-BEC product is a regridded ESA Level 2 SM data through quality filtering and quality weighting [39], which is not considered in the current evaluation. The improved SMOS-L3 SM product version 3 and the newly published SMOS-IC SM product version 2 are selected to be evaluated in this article, which are available from the Centre Aval de Traitement des Données SMOS (CATDS, at[6] and the INRAE Bordeaux website,[7] respectively. Both of the products are delivered in the NetCDF format, projected on the EASE-grid 2.0 and gridded on a 25 km spatial resolution.

The SMOS-L3 SM algorithm is a successor of the 2-parameter iteration algorithm used in the SMOS L2 but improved through a multiorbit algorithm that incorporates retrievals from several revisits over a seven day window [40]. Both of the algorithms

[6][Online]. Available: ftp://ftp.ifremer.fr
[7][Online]. Available: https://ib.remote-sensing.inrae.fr/

adopt the same complex approach to account for the pixel heterogeneous by conducting the simultaneous retrieval of SM and VOD through the iteration of the L-MEB model on the dominate fraction of land surface [11]. The key process of the algorithm is the iteration of two parameters (SM and VOD) in the L-MEB to minimize the difference between the observed and modeled TB on different incidence angles through a Bayesian cost function which accounts for the observation uncertainty, as well as a prior parameter constraints. High resolution land cover maps, optical indices (MODIS LAI), and the European Centre for Medium-Range-Weather Forecasts (ECMWF) SM data are taken to provide auxiliary information 1) in a decision tree, 2) to compute TB in the nondominant fraction of the pixel, and 3) to constrain the model inversion in the retrieval process. Prelaunch parameterization results of the soil roughness and vegetation scattering albedo are used in the L-MEB model. Main inputs of the algorithm are summarized in Table III, and more details about the algorithm can be referred to in [40].

The SMOS-IC algorithm is an alternative SMOS-L2/L3 algorithm to perform SM and VOD retrievals, which only use the surface temperature derived from the ECMWF model as auxiliary data to improve the retrieval robustness [19]. It differs from the previous SMOS-L3 algorithm in three main aspects. First, the SMOS-IC algorithm is featured by the simplified retrieval process assuming the pixel to be homogeneous, as for the AMSR2 and SMAP algorithms. Therefore, the algorithm aims at a minimal use of auxiliary data to minimize the extra uncertainties from the input data. The second revision is adopting new values of ω and soil roughness parameters, which are calibrated for different land cover types based on the IGBP classes by [17]. The new parameterization of L-MEB model are expected to improve the retrieval accuracy of SM. Last, the SMOS-IC algorithm avoids computationally expensive corrections associated to the antenna pattern and the complex SMOS viewing angle geometry in SMOS L3 algorithm, which are considered as impractical.

Data filtering is a key component in the accurate evaluation of the SMOS SM products. Currently, the root mean square error (RMSE) value between the measured and the L-MEB modeled TB data (referred to as TB-RMSE) has been widely used as an index to estimate the impact of radio frequency interferences (RFI) on the SMOS TB data [41]. In this article, the same filtering criteria considering both the scene flag information and TB-RMSE values are taken for both SMOS-L3 and SMOS-IC products [19]. First, the retrievals are filtered by considering the Scene Flag < = 1 to remove "Strong Topography," "frozen" scene, and "contaminated" scene (urban + ice + water bodies). Then, the retrievals with the TB-RMSE values > 8K are masked out to avoid areas that present strong RFI effects on SM data.

3) AMSR2 SM Products: The AMSR2 on board the GCOM-W1 satellite is the successor of AMSR-E (May 2002 to October 2011), which has been widely used to provide global SM retrieval dataset [14]. The instrument is a conical-scanning microwave imager with 14 channels at seven frequencies of 6.925, 7.3, 10.65, 18.7, 23.8, 36.5, and 89.0 GHz for both horizontal and vertical polarizations. The local overpass times of the satellite are approximately 1:30 P.M. and 1:30 A.M. for the ascending and descending orbits, respectively. In this article, four widely used

AMSR2 SM products from two different retrieval algorithms are obtained: the official JAXA SM products based on the X-band AMSR2 TB observations (hereinafter named as JAXA-X product), and three SM products using the LPRM algorithm based on 6.9 (C1 band), 7.3 (C2 band), and 10.65 GHz (X band) TB observations, hereinafter referred to as LPRM-C1/C2/X products, respectively. The former is obtained from the JAXA GCOM-W1 Data Providing Service[8] since May 2013, provided on a resolution of 0.25° in HDF5 format. The LPRM products are downloaded from the NASA's Earth Science Data Systems Program at,[9] which are delivered on the resolutions of 0.25° in HDF5 format.

The operational JAXA SM algorithm employs a lookup table to estimate SM from the AMSR2 TB observations. In the algorithm, a forward radiative transfer model is first used to generate the TB simulations under a wide range of surface (soil and vegetation) conditions for different frequencies and polarizations. Then, the SM and VWC are simultaneously estimated by utilizing two indices of polarization index (PI) and index of soil wetness (ISW), which are used to represent the normalized polarization and frequency difference between the 10 and 36 GHz TB values. The LPRM is a three-parameter (SM, VOD, and Te) retrieval model based on the multifrequency (10–36 GHz) TB observations, which is developed by Vrije University of Amsterdam in collaboration with NASA [15]. In the algorithm, the Te is derived from the vertically polarized Ka-band (36.5 GHz) observations of AMSR2 through an empirical regression model [42]. The VOD is expressed as a function of the soil dielectric constant and the microwave polarization difference index (MPDI) to avoid a reliance on additional vegetation datasets [43]. Then, the SM is finally estimated through the nonlinear iteration of the radiative transfer equation and comparisons with either C- or X-band AMSR2 TB observations. Both of the two algorithms take the simple radiative transfer model (tau-omega) as the baseline, but they differ in the simulations of the physical surface temperature, surface roughness, vegetation effects, and using different dielectric mixing models. Main inputs and key parameterizations in the algorithms are summarized in Table III, and more details can be found in [13] and [14].

D. Method

For comparison, four widely used statistical indices are used, including the Pearson correlation coefficient (R), mean Bias (bias, m^3/m^3), root mean square error (RMSE, m^3/m^3), and the unbiased RMSE (ubRMSE, m^3/m^3). The definitions are given as follows:

$$R = \frac{E[(\mathrm{SM}_{est} - E[\mathrm{SM}_{est}]) \times (\mathrm{SM}_{ref} - E[\mathrm{SM}_{ref}])]}{\sigma_{est} \times \sigma_{ref}}$$

$$\mathrm{Bias} = E[\mathrm{SM}_{est}] - E[\mathrm{SM}_{ref}]$$

$$\mathrm{RMSE} = \sqrt{E[(\mathrm{SM}_{est} - \mathrm{SM}_{ref})^2]}$$

$$\mathrm{ubRMSE}$$
$$= \sqrt{E[((\mathrm{SM}_{est} - E[\mathrm{SM}_{est}]) - (\mathrm{SM}_{ref} - E[\mathrm{SM}_{ref}]))^2]}$$

[8][Online]. Available: https://gportal.jaxa.jp/gpr/
[9][Online]. Available: https://search.earthdata.nasa.gov/

LPRM-C1 LPRM-C2 LPRM-X JAXA-X SMOS-IC SMOS-L3 SMAP-SCAH SMAP-SCAV SMAP-DCA
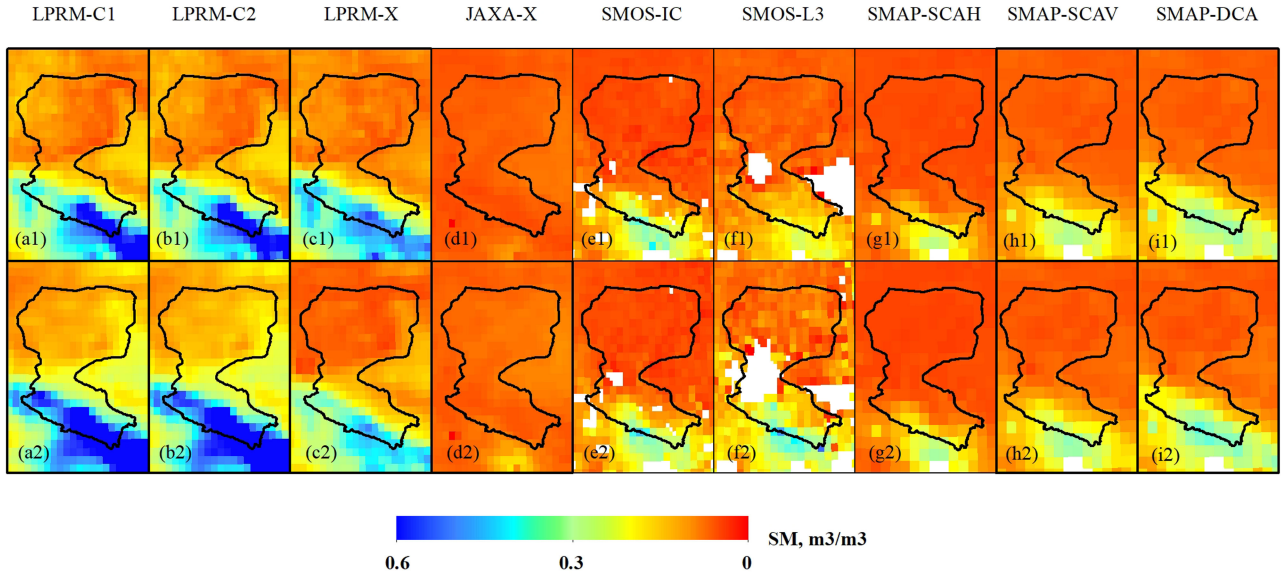

Fig. 2. Spatial distributions of AMSR2, SMOS, and SMAP soil moisture products in both AM [(a1)–(i1)] and PM [(a2)–(i2)] orbits, averaged during the unfrozen seasons of 2015 in HRB.

where SM_{est} and SM_{ref} represent the satellite-based and *in situ* SM observations, respectively; $E[\bullet]$ and σ are the expectation and standard deviations in mathematics. Here, the R value is used to depict the ability of SM_{est} in capturing the temporal variation of the in-situ SM observations, bias reflects the wetness or dryness degree of the SM_{est} compared to SM_{ref}; RMSE represent the absolute mean deviation of time-series SM_{est} to SM_{ref}, while the ubRMSE represent the relative deviation of SM_{est} to SM_{ref} after eliminating the bias in RMSE.

Data preprocessing is taken for both *in situ* and remotely sensed datasets to ensure their spatiotemporal consistency in the evaluation. Spatially, the multiple surface SM observations within the satellite pixels are then arithmetically averaged to make up the spatial discrepancy between the *in situ* and satellite data [44]–[46]. The distribution of the observation nodes in each evaluation sites are plotted in Fig. 1 and the numbers are summarized in Table I. Temporally, the ground SM observations at the depth of 0–5 cm are first filtered within a 1-ho windows before and after the equatorial overpass time and then averaged to ensure the temporal consistency between the *in situ* and satellite data. The fair comparisons of the satellite-based SM retrievals with the ground SM observations are currently conducted during the unfrozen seasons from 2013 to 2017, except for the SMAP SM products (three years from 2015 to 2017). In this research, the widely used discrimination method is taken to define the unfrozen seasons as the days when the surface mean soil temperature above 0 °C [25]. Similar data preprocessing is also taken for the Ts observations.

Last, the descending AMSR2 and SMAP products at the local overpass time of 1:30 am and 6:00 am, and the ascending SMOS products at 6:00 am are referred to as AM-orbit products, and the others are referred to as the PM-orbit products in the following discussion for simplification.

Fig. 3. Time series of AMSR2 daily SM retrievals in AM orbit with the ground SM observations during the unfrozen period from 2013 to 2017 for three evaluation sites in HRB.

III. RESULTS

In this section, results of the nine satellite-based SM products for each evaluation site in HRB are discussed individually. Fig. 2 compares the spatial distributions of the averaged SM during the unfrozen seasons in 2015 in HRB from different products at both AM- and PM-orbit overpass times. Fig. 3 exhibits the temporal behaviors of four AMSR2 SM products (LPRM-C1/C2/X and JAXA-X products) through time series comparisons with the ground SM observations from
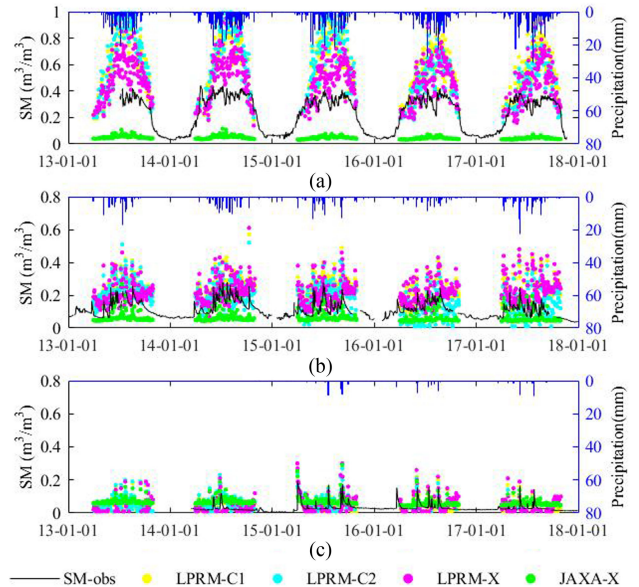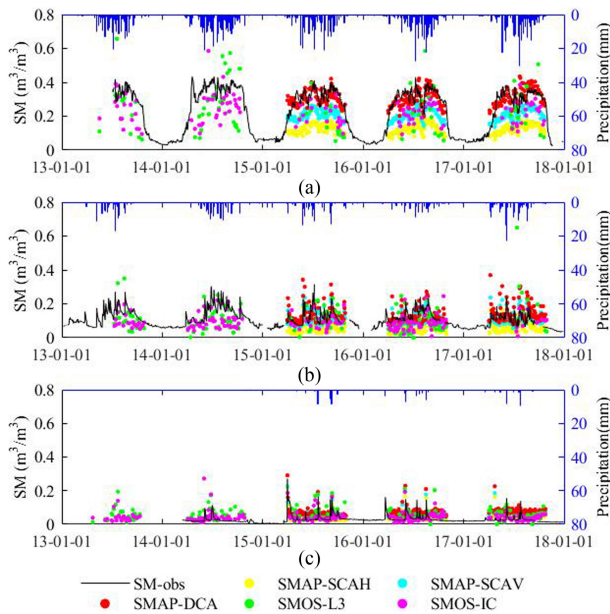
Fig. 4.   Time series of daily SMOS and SMAP SM products in AM orbit with the ground SM observations during the unfrozen period from 2013 to 2017 for three evaluation sites in HRB.

2013 to 2017 at the three evaluation sites of up-, mid-, down-HRB, respectively. Similar temporal behaviors of five L-band passive microwave remotely sensed SM products (SMOS-IC, SMOS-L3, and SMAP-SCAH/SCAV/DCA) with ground observations from 2013 to 2017 at the evaluation sites are exhibited in Fig. 4. All the statistic values are then summarized in Table IV.

A. Evaluation in the Up-HRB Site

In the up-HRB validation site, alpine meadow covers up to almost 80% of the land. The annual mean precipitation is around 438 mm, and most of the precipitation occurs during the monsoon season from May to October according to the observations in both Figs. 3 and 4. The observed SM values correspond well to the variation in precipitation, resulting in the relatively high SM values and large extend in seasonal SM variation in up-HRB site. Temporally, the SM values increase rapidly from around 0.2 to 0.4 m^3/m^3 in early April, and maintain consistently as high as around 0.4 m^3/m^3 from late April to September, and then decrease to about 0.2 m^3/m^3 in late October in general.

Time series of AM-orbit satellite-based SM retrievals and the corresponding ground SM observations in up-HRB site are compared in Figs. 3(a) and 4(a). The statistics for both the AM-orbit and PM-orbit data are summarized in Table IV. For the C-band and X-band AMSR2 products in Fig. 3(a), the three AMSR2 LPRM products can roughly reflect the seasonal dynamic of SM with temporal correlation coefficient of ∼0.45, while obviously large overestimation are observed in the retrievals. The X-band LPRM product gain superiority to the C-band products with the slightly improved R values and the much lower biases of ∼0.17 m^3/m^3. However, the still high ubRMSE above 0.15 m^3/m^3 poses an obstacle in their applications. The JAXA-X

product achieves the lowest ubRMSE of ∼0.05 m^3/m^3 as well as the comparable temporal R values of ∼0.44 among the four AMSR2 products. However, the JAXA-X SM retrievals present great underestimation biases of ∼0.28 m^3/m^3, which constrains their effective applications in hydrological model simulations. In the analogical evaluation of SMOS and SMAP products in Fig. 4(a), similarly high overall accuracy of ubRMSE within 0.04 m^3/m^3 is observed for all the three SMAP SM products. Individually, the SMAP-SCAH and SMAP-SCAV gain slightly superiority in reflecting temporal dynamics of SM variations with the highest R values of ∼0.70. However, systematic underestimations above 0.10 m^3/m^3 are observed, and the underestimation biases are much larger for SMAP-SCAH product (∼0.19 m^3/m^3) than the SMAP-SCAV product. The SMAP-DCA SM retrievals achieve the best performance with high R values above 0.65, low ubRMSE within 0.04 m^3/m^3, as well as the lowest underestimation bias of ∼0.01 m^3/m^3 in up-HRB site. However in applications, the short period of SMAP data available since 2015 would be a restriction in their long-term analyses, which calls for the urgency of data fusions.

Great diversity is observed in the evaluation results of the two SMOS SM products. The newly published SMOS-IC product gains much superiority to the previous SMOS-L3 product with the higher temporal correlation coefficient values of ∼0.56 and much improved ubRMSE of ∼0.07 m^3/m^3. While in biases, similar underestimations of ∼ 0.10 m^3/m^3 are observed for both SMOS-IC and SMOS-L3 SM products in the up-HRB site, which is comparable to the underestimation of SMAP-SCAV product and much lower than the underestimation of SMAP-SCAH and JAXA-X products. However in applications, both the SMOS-IC and SMOS-L3 products are suffering from severe RFI contamination during the study period in this region. According to the statistics in Table IV, more than 75% of the SMOS SM retrievals have been filtered in the process of data quality control. As a result, the small number of SMOS SM retrievals would be a main restriction in their applications in this region.

For the PM-orbit data, the similar but much worse evaluation results are observed in Table IV. These findings are generally in accordance with previous researches, which also found a general overestimation of LPRM SM products as well as the slightly improved performance of the AM-orbit data over the Qinghai-Tibet Plateau [25], [27] and Genhe river basin [47] in China. The worse performances of PM-orbit data are generally considered to be related to the decreased thermal equilibrium conditions of the near-surface air, vegetation canopy, and surface soil during day or afternoon times [44]. Another finding in Table IV is the more SMOS SM retrievals filtered in the PM-orbit data. The TB-RMSE is currently widely used as an index to estimate the impact of RFI on the SMOS TB data [19]. According to the comparison of temporal averaged TB-RMSE for both ascending and descending SMOS-IC data during the evaluation period from 2013 to 2017 in Fig. 5, the annual mean TB-RMSE values are generally above 10 K for the descending orbit SMOS data in HRB. This results in the more RFI-contaminated retrievals to be filtered, which also contribute to the decreased temporal correlations in comparison to the AM-orbit data in the evaluations.

TABLE IV

PERFORMANCE METRICS OF AMSR2, SMOS, AND SMAP SOIL MOISTURE PRODUCTS DURING UNFROZEN SEASONS FROM 2013 TO 2017 FOR THREE EVALUATION SITES IN HRB

Evaluation Sites	Product	AM-orbit SM products					PM-orbit SM products				
		R	Bias	RMSE	ubRMSE	N	R	Bias	RMSE	ubRMSE	N
Up-HRB	LPRM-C1	0.43	0.29	0.35	0.20	666	0.36	0.43	0.46	0.17	733
	LPRM-C2	0.45	0.27	0.34	0.21	666	0.34	0.41	0.46	0.20	733
	LPRM-X	**0.47**	**0.17**	**0.22**	0.15	666	0.29	**0.11**	**0.16**	0.12	733
	JAXA-X	0.44	-0.28	0.28	**0.05**	730	**0.49**	-0.26	0.27	**0.05**	734
	SMOS-IC	**0.56**	-0.10	**0.12**	**0.07**	123	0.28	-0.08	**0.10**	**0.07**	92
	SMOS-L3	0.25	**-0.08**	0.16	0.14	99	**0.39**	**-0.06**	0.12	0.10	38
	SMAP-SCAH	0.68	-0.19	0.19	0.04	289	0.53	-0.22	0.22	**0.04**	262
	SMAP-SCAV	**0.70**	-0.10	0.11	**0.03**	289	0.56	-0.13	0.14	**0.04**	262
	SMAP-DCA	0.66	**-0.01**	**0.04**	0.04	289	**0.59**	**-0.04**	**0.06**	0.05	262
Mid-HRB	LPRM-C1	**0.42**	0.11	0.13	0.07	766	0.18	0.14	0.16	0.08	742
	LPRM-C2	0.34	**0.06**	0.10	0.08	718	0.15	0.10	0.14	0.10	743
	LPRM-X	0.26	0.09	0.12	0.08	766	-0.01	**0.01**	**0.08**	0.08	744
	JAXA-X	0.29	-0.07	**0.08**	**0.05**	739	**0.33**	-0.08	0.09	**0.05**	735
	SMOS-IC	**0.40**	-0.04	**0.07**	**0.05**	159	0.22	-0.06	**0.08**	**0.05**	118
	SMOS-L3	0.24	**-0.02**	0.09	0.08	144	**0.28**	**0.00**	0.10	0.09	104
	SMAP-SCAH	**0.40**	-0.07	0.08	**0.04**	278	**0.46**	-0.07	0.08	**0.04**	269
	SMAP-SCAV	0.38	**-0.01**	**0.05**	0.05	278	0.44	-0.02	0.05	**0.04**	269
	SMAP-DCA	0.32	0.01	0.06	0.05	278	0.42	**0.01**	**0.05**	0.05	269
Down-HRB	LPRM-C1	**0.41**	**0.02**	0.05	0.04	352	0.10	0.10	0.12	0.05	706
	LPRM-C2	0.39	0.03	0.05	0.04	303	0.14	0.09	0.11	0.07	642
	LPRM-X	0.39	0.02	0.05	0.05	372	-0.07	0.05	0.07	0.04	705
	JAXA-X	0.24	0.03	**0.04**	**0.03**	685	**0.32**	0.04	**0.05**	**0.03**	696
	SMOS-IC	**0.27**	**0.01**	**0.04**	**0.04**	202	**0.10**	**0.00**	**0.03**	**0.03**	146
	SMOS-L3	0.13	0.02	0.05	0.04	182	0.07	0.03	0.06	0.05	137
	SMAP-SCAH	**0.34**	**0.002**	**0.03**	**0.03**	319	**0.43**	**0.0005**	**0.03**	**0.03**	293
	SMAP-SCAV	0.25	0.03	0.04	0.03	319	0.41	0.02	0.04	0.03	293
	SMAP-DCA	0.28	0.03	0.05	0.03	319	0.42	0.03	0.05	0.03	293

B. Evaluation in the Mid-HRB Site

In the mid-HRB site, the landscape is composed by the complex underlying surface of desert-artificial oasis compound. The artificial oasis makes up ∼43% of the landscape and corn fields cover up to ∼80% of the oasis. The annual mean precipitation decreases to 147 mm according to observations in the mid-HRB site, and the precipitation events mostly occur during the monsoon season from May to October, resulting in the seasonal variated SM observations generally ranging from about 0.1 to 0.4 m³/m³ during the unfrozen seasons. However, due to the frequent irrigation events conducted in the artificial

oasis, the variations of ground SM observations correspond partially to the daily precipitation events, and more fluctuations and larger variation scopes are observed in SM variations than the precipitation changes shown Figs. 3(b) and (b).

The overall overestimation of the LPRM-C1/C2/X SM products, and the general underestimation of the JAXA-X, SMOS-IC/L3, SMAP-SCAH/SCAV SM products are also depicted in Fig. 3(b) over the mid-HRB site for the AM-orbit data. However, the overestimation/underestimation biases are entirely smaller than that for the grassland in the up-HRB site. In terms of temporal correlations, much lower R values (∼0.30 for the
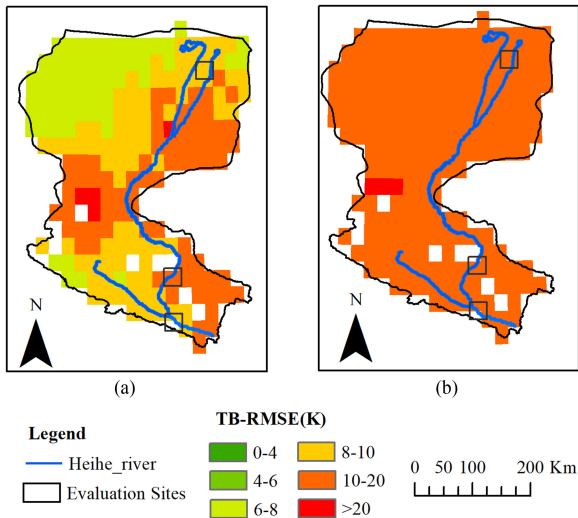
Fig. 5.　Comparison of temporal averaged TB-RMSE values in HRB for both (a) AM-orbit and (b) PM-orbit SMOS-IC data during the evaluation period from 2013 to 2017.

JAXA-X, SMOS-L3, and SMAP-DCA products, ~0.35 for the LPRM-C1, C2, X products, ~0.4 for SMAP-SCAH, SCAV, and SMOS-IC products) are also observed in the mid-HRB site. One possible reason could be explained by the complex landscapes and the frequently irrigation incidents during the validation period in the mid-HRB site. The more heterogeneous SM distributions and limited sampling observations in the validation site increase the difficulties to obtain the accurate "proxy" of the ground truth to be compared with the pixel-size satellite SM retrievals. The overall accuracy of all the SM products can be ranged as SMAP-SCAH/SCAV/DCA, SMOS-IC, JAXA-X (0.05 m^3/m^3) > SMOS-L3, LPRM-C1/C2/ X (0.08 m^3/m^3) in ubRMSE for the moderate vegetated land cover regions in the mid-HRB site. Compared to the ubRMSE values for the dense grassland in the up-HRB site, the accuracy of three SMAP SM products are slightly decreased in the mid-HRB site, which could also be attributed to the more complex land cover types as well as the more heterogeneous SM distributions in the mid-HRB regions. However, the accuracies of the three LPRM SM products are much improved in the mid-HRB site, which could be related to the greatly improved simulations of vegetation conditions discussed in the following Section IV-A.

For the PM-orbit data, the general decreased temporal correlations and larger ubRMSE values are also observed compared to the AM-orbit data. The PM-orbit LPRM SM products behave even worse in reflecting the temporal variations of the ground SM observations (R < 0.2). Especially, a reverse temporal pattern (R = −0.01) with the ground SM observations is observed in the LPRM-X SM retrievals shown in Table IV. The abnormal situations are also observed in Qinghai-Tibet plateau [27], which could be related to the poor estimation of VOD in the LPRM algorithm during the year except for summer seasons [48]. Oppositely, the three SMAP SM products present similarly high accuracy of ~0.04 m^3/m^3 in ubRMSE and the even better temporal correlations with R values above 0.4 than the results for the AM-orbit data in the mid-HRB site.

C. Evaluation in the Down-HRB Site

In the down-HRB site, the low-vegetated desert and the sparsely vegetated natural oasis make up the main landscape. The annual mean precipitation decreases to an extremely low level below 50 mm according to the observations from AWS stations. The precipitation events occasionally happened in summer and autumn with small amount, resulting in the generally low SM measurements below 0.05 m^3/m^3 during the year and the occasional fluctuations with sharp increasing and gradual decreasing varying between about 0.03 to 0.2 m^3/m^3 during a few days after the precipitation occasions.

Ground SM variations corresponding quite well with the precipitation events in the down-HRB site in Figs. 3(c) and 4(c). High accuracy of ubRMSE within 0.04 m^3/m^3 is observed for all the LPRM-C1/C2/X, JAXA-X, SMOS-IC, and SMAP-SCAH/SCAV/DCA SM products in Table IV. The LPRM products present the reliable capability in reflecting the SM variations with R values of ~0.40. However, the SMOS and SMAP SM retrievals can hardly capture the temporal SM variations in ground observations at the AM-orbit overpass time. Considering the extremely dry soil in the down-HRB, the L-band microwave signals would correspond to a much deeper soil emitting layer, and the ground SM observations are obtained at a fixed depth of 5 cm. The mismatch of detective depths between the SM retrievals and observations could be one of the main reasons explaining the low temporal correlation R values in this evaluation. For the PM-orbit data, the much decreased temporal correlation R values are also observed in the PM-orbit SMOS SM products. In contrast, the PM-orbit SMAP SM products reflect the seasonal SM variations better with slightly higher R values than the AM-orbit data.

IV. DISCUSSIONS

Table III summarizes the main components in the operational SM retrieval algorithms of SMAP-SCAH/SCAV/DCA, SMOS-L3/IC, JAXA, and the LPRM products. According to the sensitivity analysis of parameters used in radiative transfer model, surface temperature, roughness, and VOD apart from SM make the three main factors affecting the simulated TB in the SM retrieval algorithms [49]. Surface roughness is an abstract factor describing the surface elevation fluctuations in the retrieval pixels, which is rather stable over time and difficult to be quantified directly [50]. In this article, surface temperature and VOD are evaluated in details, with the time series of daily layered soil temperature observations from *in situ* networks and 16-day averaged NDVI data from MODIS taken as references.

A. Vegetation Optical Depth

Vegetation effects are a vital element affecting the reliable SM retrievals from satellite observations, which should be accounted for carefully in the forward radiative transfer model. In the simplified tau-omega model, the vegetation effects are evaluated through two parameters of ω and VOD, which are used to simulate the vegetation scattering and extinction, respectively. In most operational low frequency microwave SM algorithms, ω is generally set to a constant small value, making VOD the
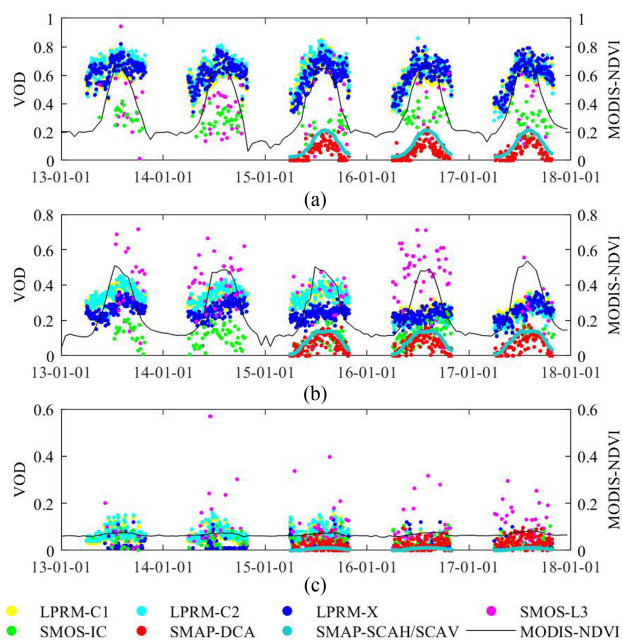
Fig. 6. Time series (2013–2017) of daily AM-orbit VOD retrievals in SMOS, SMAP, and AMSR2 LPRM products with the MODIS NDVI observations over the three evaluation sites in HRB.

Fig. 7. R values between the time series (2013–2017) of AM-orbit VOD retrievals and MODIS NDVI over the three evaluation sites in HRB.

most influential factor to be considered [18]. According to the algorithm comparison in Table III, the AMSR2 LPRM, SMOS 2-parameters, and SMAP DCA algorithms simultaneously obtain VOD and SM retrievals in their iteration processes, owing to their multichannel TB observations from different polarizations and incidence angles, respectively. The MODIS NDVI climatology is used as reference in the SMAP-SCAH/SCAV algorithms to obtain their VOD simulations through a linear relationship. No VOD are retrieved in the AMSR2 JAXA algorithm.

Time series of MODIS NDVI data are selected as a proxy to evaluate the performance of VOD retrievals from different algorithms. According to the temporal comparisons of VOD retrievals and NDVI series over three validation sites in the HRB shown in Fig. 6, the VOD values retrieved in the SMOS, SMAP, and LPRM algorithms roughly reflect the spatial variation of vegetation greenness/growth, and the VOD retrievals generally increase as the annual NDVI increase from around 0.1 to 0.4 from down- to up-HRB sites. However, large differences exist in terms of the absolute VOD values among different products. Generally, much higher VOD retrievals are achieved in the LPRM products than the SMOS and SMAP products. The differences are mainly resulted from the different sensor configuration and algorithm settings [51]. For one thing, the longer frequency of L-band indicates the deeper penetration depth inside the vegetation canopy and more information from the deeper canopy in the SMOS and SMAP VOD retrievals than the LPRM data. For another, the SM and VOD simultaneously retrieved in the multiparameter retrieval algorithms based on multi-incidence angle/polarization TB observations are strongly correlated, resulting in the ill-posed problems in the VOD retrievals. The empirical relationship of VOD = b ∗ VWC are frequently used to improve the VOD retrievals by constraining
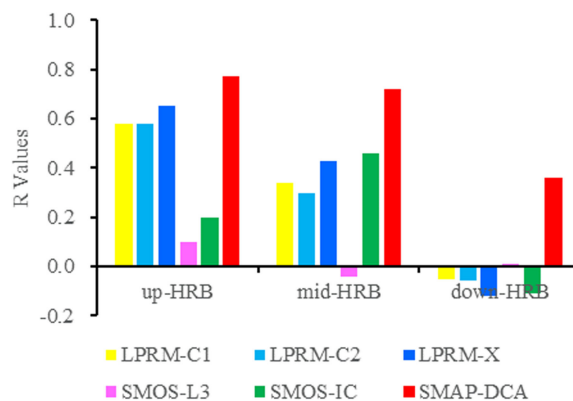
the initial guess of VOD in the iteration of tau-omega model in the current SMOS/SMAP multiparameter retrieval algorithms. However, no priori information is referred in the LPRM algorithm, and the VOD are retrieved based on the MPDI through an analytical method. Consequently, dense vegetation condition with high VOD approaching 1 would be achieved when the MPDI decreases to near zero, resulting in the large uncertainty in the present LPRM VOD retrievals, especially over the dense vegetation [52].

The correlation coefficient values between the MODIS NDVI and different VOD series over three validation sites in HRB are then summarized in Fig. 7. According to the statistics, the X-band LPRM VOD retrievals reflect the temporal variation of NDVI series better than the C-band results, with high temporal correlation values above 0.6 for densely vegetated grassland in up-HRB site and slightly lower R values of around 0.45 for moderately vegetated regions in the mid-HRB site. The high VOD retrievals in LPRM products are related to the great overestimation of SM retrievals observed in Fig. 3. According to the theoretical analyses of radiative transfer process in the LPRM algorithm, high VOD retrievals indicate the low transmissivity of vegetation canopy as well as the high vegetation emissivity, resulting in a decreased soil emissivity together with the increased soil dielectric constant and eventually the increased SM values based on the soil dielectric model. The results are in line with the previous findings that the correction of vegetation effects should be improved in LPRM algorithms, especially over the dense vegetated areas [27].

The VOD retrievals from the SMOS product present larger fluctuations than those from both LPRM and SMAP products, especially the SMOS-L3 product. The fluctuations are also observed in their SM retrievals in Fig. 4, which could be related to the well-known RFI effects during the validation period in China. The situation can be much improved in the future as a strong decrease of RFI effect has been observed over China after 2016 in [19] and a stricter criterion in RFI filtering can also be taken to further improve the temporal stability of VOD and SM retrievals from the SMOS TB observations. Much lower correlations with NDVI is observed for SMOS VOD retrievals (R values < 0.1 for the SMOS-L3 VOD retrievals and R values

< 0.5 for the SMOS-IC retrievals) compared to that for the LPRM products, especially over the high mountainous up-HRB evaluation site. The situation is understandable as it has been widely recognized that the vegetation information reflected in VOD retrievals and optical vegetation indexes are frequency dependent [51]. The penetration capabilities of the microwave radiations within the canopy layer increase as the frequency decreases. As a result, the lower frequencies (L-band) VOD retrievals are sensitive to the water content present in the whole vegetation layer including the woody components of the vegetation, which correspond more to the property of above ground biomass. While higher frequencies (C- and X-band) observations are more sensitive to the water content of the upper layer of the vegetation canopy and, consequently, to the green vegetation components (leaves and stems for herbaceous vegetation, crown, and leafy part of trees in forests), which correspond more to the optical vegetation indexes such as NDVI, LAI, EVI, and so on [41]. Consequently, the C- and X-band VOD retrievals in LPRM products correlate more with NDVI than the SMOS product, and correlations are even higher for the X-band LPRM product than that for the C-band product. Obviously higher temporal correlations between VOD retrievals and NDVI are observed for the SMOS-IC VOD retrievals than the SMOS-L3 data, and the correlations are even better (∼0.50) for the AM-orbit SMOS-IC product over the low vegetated cropland in the mid-HRB site. The result is in line with the previous analyses that the NDVI as a proxy of L-band VOD values are more applicable for herbaceous vegetation [19].

The SMAP-DCA product gets the lowest VOD values for both vegetated and bare soil regions in HRB. However, the strongest correlation between the SMAP VOD and NDVI values are obtained in their retrievals compared to the LPRM and SMOS data, with the mean R values above 0.7 for SMAP-DCA product, and around 0.97 for SMAP-SCAH/SCAV products over all the three validation sites. The high correlation R values are reasonable, as the MODIS NDVI climatology is introduced in the initial guessing of VOD in their iterations in the SMAP DCA algorithm [51]. To be noted, the VOD retrievals in SMAP-DCA product are comparable to those from the SMOS-IC product in the mid- and down-HRB sites, while obviously lower VOD retrievals are observed in the up-HRB site. Considering the obviously underestimation biases in SMOS-IC/L3 and SMAP-SCAH/SCAV SM products, new parameterization schemes of VOD relying on the optical NDVI dataset need to be improved for alpine meadows in the future.

B. Temperature of the Emitting Layer

The temperature of the emitting layer is a key parameter in the tau-omega model for estimating SM and its calculation is a key step in SM retrieval algorithms [18]. As listed in Table III, The LPRM algorithm estimates the surface temperature through a linear relationship between Te and the vertical polarization brightness temperature at 36.5 GHz [42]. While the JAXA algorithm takes the PI and the ISW in SM retrieval to minimize the effect of Te, and a constant value of 293 K is applied throughout

the year globally [14]. Considering the lower sampling depth (< 5 cm) of effective soil temperature in the C/X-band satellite observations, the Ts values for the top 5 cm soil layer (Ts_surf) obtained from the ground observation networks are selected in the evaluation of the Te inputs from the AMSR2 LPRM and JAXA products.

Deeper sampling depths (< 5 cm) of effective soil temperature are taken in the L-band satellite observations. A two-layer algorithm is taken to estimate the Te values in the SMOS and SMAP algorithms. In the algorithms, two layers of the soil physical temperature (Ts_surf, Ts_deep) are obtained from the datasets of the ECMWF [11] and the GEOS-5 model simulations [46], respectively. However in the evaluations, only the Ts for the first layer (approximately between 1 and 5 cm) from ECMWF is provided in both SMOS-L3 and SMOS-IC products. Consequently, the Ts_surf observations for the top-5 cm soil layer are also selected in the evaluation of Ts inputs in the SMOS products. The Te values provided in the SMAP-DCA product are simulated based on the modeled soil temperature for both first (approximately between 1 and 10 cm) and second (approximately between 10 and 20 cm) soil layers in GEOS-5 model. The in site Ts observations at two different depths of 5 and 20 cm are selected to estimate the ground observed Te (according to the simplified parameterization scheme of Te in [53]) in the evaluation of SMAP-DCA Te inputs. Besides, for the consistency in comparison, the evaluation of Te inputs in SMAP-DCA algorithm is also conducted based on Ts_surf (0–5 cm) observations.

The temporal comparisons of the Te inputs in the LPRM/SMOS/SMAP products with the ground observations are exhibited in Fig. 8 (Ts_surf for 0–5 cm layer is used as proxy), and the corresponding statistics are summarized in Table V. It is observed in Fig. 8 that all the LPRM/SMOS/SMAP Te inputs reflect the seasonal variation in Te ground observations, with high temporal correlation R values above 0.7 for both the AM- and PM-orbit data. The LPRM Te inputs present underestimation for the AM-orbit data, and the underestimation biases are much higher for the less vegetated evaluation regions in the mid- and down-HRB sites. While the LPRM Te inputs generally show overestimations for the PM-orbit data, and the overestimation biases are larger for the dense vegetated up-HRB regions. In terms of temporal correlation, the AM-orbit LPRM Te input correspond to the ground Te observations better, with slightly higher temporal correlation R values generally above 0.8. One possible reason could be explained that the Te retrievals in the LPRM algorithm represent the land surface temperature incorporating both the soil temperature and the overlaying vegetation temperature. However, different thermal equilibrium conditions are achieved at the descending and ascending overpass time of 1:30 AM and 1:30 PM for the AMSR2 satellite, which roughly correspond to the lowest and highest temperature of the day, respectively. The differences between the canopy and soil temperature have been proved to be higher at the PM-orbit overpass time than the AM-orbit time, and the hypothesis of the hydraulic quasi-equilibria of Tv = Te in the LPRM algorithms are more reasonably for the AM-orbit data.
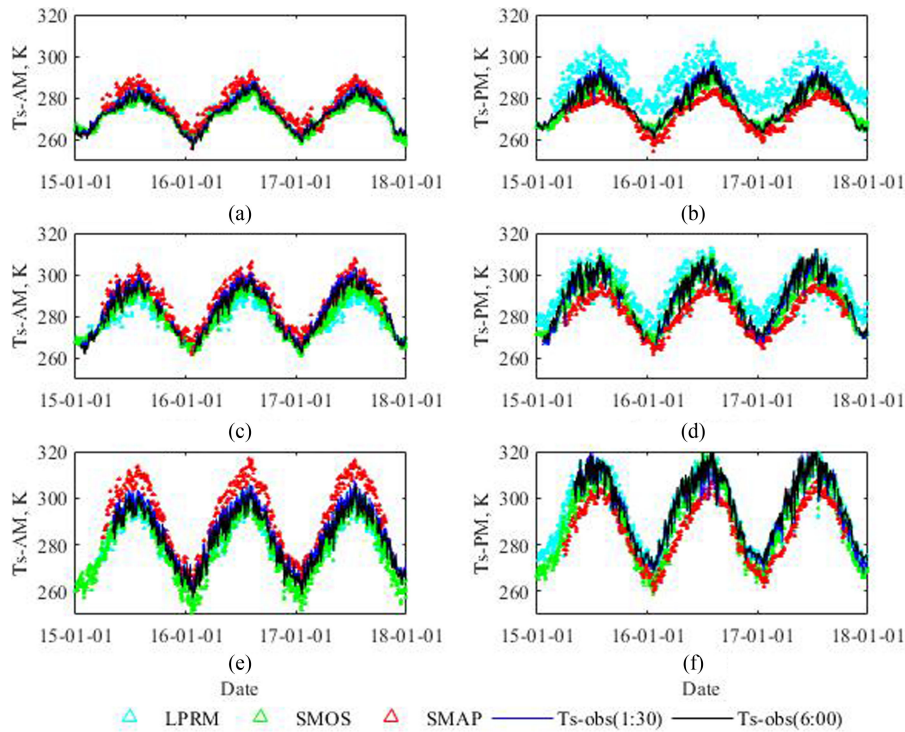
Fig. 8. Time series of the surface soil temperature of the emitting layer (Ts_surf, K) from different SM products in both AM and PM orbit with ground observations during 2015 to 2017 over the three evaluation sites in HRB.

TABLE V
PERFORMANCE METRICS OF TE INPUTS FOR THE SM PRODUCTS DURING THE UNFROZEN SEASONS IN 2015–2017 OVER THREE EVALUATION SITES IN HRB

Date	Validation Sites	Te in LPRM vs. Ts_surf			Te in SMOS vs. Ts_surf			Te in SMAP vs. Ts_surf			Te in SMAP vs. Ts_eff		
		R	Bias	N	R	Bias	N	R	Bias	N	R	Bias	N
AM-orbit	Up-HRB	0.83	0.23	422	0.95	-0.95	640	0.85	4.36	308	0.88	2.98	308
	Mid-HRB	0.82	-7.28	437	0.91	-2.70	557	0.82	4.26	269	0.85	2.77	269
	Down-HRB	0.91	-6.02	495	0.82	-7.28	437	0.89	10.99	303	0.93	6.50	303
PM-orbit	Up-HRB	0.79	7.93	477	0.94	-1.68	641	0.87	-6.16	299	0.94	-3.65	299
	Mid-HRB	0.75	2.68	419	0.90	-2.98	560	0.75	-10.92	260	0.91	-6.44	260
	Down-HRB	0.95	-0.43	504	0.75	2.68	419	0.82	-11.28	278	0.94	-5.39	278

Both the SMOS and SMAP Te inputs present improved performance than the LPRM data, with the decreased over-estimation/underestimation biases and the increased temporal correlation values. The SMOS Te input presents the highest R values above 0.9 and lowest mean biases below −3 K for the vegetated regions in both up- and mid-HRB evaluation sites. One possible reason could also be related to more uniform soil dielectric properties among different soil layers and the approximate temperature between canopy and soil during the ascending overpass time of SMOS at 6:00 AM. For another, the consistent underestimation of Te inputs observed in SMOS data could be one reason explaining the overall underestimation of SMOS SM retrievals for vegetated land cover types shown in Table IV. Theoretically, in the forward microwave emission model, the

underestimation of Te values in SM retrieval algorithm will result in the overestimation of soil emissivity together with the underestimation of soil reflectivity, which will eventually lead to an underestimation in SM retrievals, as discussed in [32].

In contrast to the LPRM data, the SMAP Te inputs present overestimation biases for the AM-orbit data and underestimation biases for the PM-orbit data, and the temporal correlation R values are slightly higher for the PM-orbit data. As for the land cover types, much lower overestimation biases are observed for the vegetated land cover types in the up- and mid-HRB sites for the AM-orbit SMAP data, and obviously higher overestimation/underestimation biases are observed for the low-vegetated down-HRB site. However, considering the entirely higher underestimation biases of the SMAP-SCAH and

the SMAP-SCAV SM products than the SMAP-DCA product for the vegetated HRB regions in Table IV, the systematic overestimation/underestimation biases of Te inputs in SMAP algorithm should not be the main reason leading to the general underestimation biases in SMAP-SCAH/SCAV SM retrievals.

To be noted, the current evaluation of Te is mainly conducted based on the Ts_surf (0–5 cm) observations from the SMSTS in the HRB. However, researches have confirmed the varying sampling depth in effective SM simulations, which is varying depends on both frequencies and SM. For one example, the deeper sampling depth of ∼15 cm in L-band Te simulations has been confirmed during the unfrozen season over a Tibetan meadow site based on the long-term diurnal brightness temperature observations collected by the ELBARA-III radiometer [54]. The similar sampling depth would also be found over the up-HRB site under the similar geographic conditions. Improved evaluation results are achieved when the soil temperature from the deep soil layer is considered in the evaluation of SMAP-DCA product in Table V, indicating the difference between the sampling depths between the Te simulations in satellite products and *in situ* observations to be further considered in the future evaluation of L-band SM retrievals.

V. CONCLUSION

In this article, nine recently developed versions of passive microwave remotely sensed SM products (SMOS-IC, SMOS-L3, SMAP-SCAH/SCAV/DCA, AMSR2 LPRM-C1/C2/X, and AMSR2 JAXA) are detailed evaluated and intercompared against the ground observations from the distributed observation networks established in HRB under diverse land surface conditions for a long time series from 2013 to 2017. The uncertainties of two affecting factors in the retrieval algorithms, namely the physical surface temperature and VOD are analyzed to conduct the error source analyses based on the synchronous ground soil temperature observations and the supplementary vegetation observations from MODIS NDVI. The important findings are concluded as follows:

The SMAP-SCAH/SCAV/DCA SM retrievals reflect the seasonal variations in the HRB well with comparably high temporal correlations of ∼0.7 over the dense vegetated regions in the HRB, and present high accuracy within 0.04 m³/m³ in terms of ubRMSE. The SMAP-DCA product gains superiority to the SMAP-SCAH/SCAV products with obviously lower underestimation biases. The SMOS-L3 SM retrievals present uneven fluctuations and show increased underestimation between −0.02 and −0.13 m³/m³ as the vegetation conditions increase and ubRMSE errors of ∼0.10 m³/m³ in the HRB. The SMOS-IC product presents large improvement *vs* the SMOS-L3 data with increased temporal correlations above 0.4 and lower ubRMSE of ∼0.05 m³/m³. The three LPRM products show very large overestimation over the vegetated HRB. The X-band LPRM SM retrievals in descending orbit at 1:30 AM present better performance than the C-band data with increased overestimation biases between 0.09 and 0.17 m³/m³ and ubRMSE errors from 0.08 to 0.15 m³/m³ as the vegetation effects increase. The JAXA-X SM retrievals show high accuracy within 0.05 m³/m³ in terms of ubRMSE. But the retrievals present extremely

high underestimation over the dense vegetated grassland in the upstream HRB.

High precisions of mean biases within −3K are obtained for physical soil temperature of the emitting layer in the SMOS algorithms, indicating that the uncertainties in Te inputs may affect the accuracy of the SMOS SM retrievals, but should not be the leading factor. The overestimation/underestimation biases in Te inputs over the HRB are related to the mismatch of the sampling depths between the Te simulations in satellite products and ground Te observations, calling for the better representative of sampling depths in the simulation of Te in the future evaluations. Correction of vegetation effects should be further improved in the current LPRM, SMOS, and SMAP algorithms. The extremely high VOD retrievals in LPRM products over the dense vegetated regions in HRB could be one reason resulting in the large overestimation in the SM retrievals. The uneven fluctuations in SMOS VOD retrievals should be much reduced in the future as the well-known RFI contamination effects in China are strongly decreasing since 2016. The obviously larger underestimation biases in SMAP-SCAH/SCAV SM products than the SMAP-DCA product indicate the possible error resources in their parameterization scheme. Considering the different vegetation information reflected in microwave VOD and optical vegetation indexes, it is expected the current parameterization scheme of VOD relying on the optical NDVI dataset to be further improved in the future.

The superior evaluation performance of the SMAP-DCA product in the HRB guarantees its applications in water budget and energy balance analysis. However, the SMAP SM products are limited by the short period of data acquisition since 2015. Future works on obtaining a long-term, accurate SM dataset in HRB call for the effective combination of AMSR2, SMOS, and SMAP SM products. This research is expected to provide insight into the improvement of products based on the revision of both surface temperature and vegetation correction, as well as other factors like dielectric mixing model and surface roughness model comprehensively in the future.

REFERENCES

[1] B. Martens, D. G. Miralles, H. Lievens, D. Fernandezprieto, and N. Verhoest, "Improving terrestrial evaporation estimates over continental Australia through assimilation of SMOS soil moisture," *Int. J. Appl. Earth Observ. Geoinf.*, vol. 48, pp. 146–162, 2016.
[2] S. Sadri *et al.*, "A global near-real-time soil moisture index monitor for food security using integrated SMOS and SMAP," *Remote Sens. Environ.*, vol. 246, 2020, Art. no. 111864.
[3] A. K. Mishra, T. Vu, A. V. Veettil, and D. Entekhabi, "Drought monitoring with soil moisture active passive (SMAP) measurements," *J. Hydrol.*, vol. 552, pp. 620–632, 2017.
[4] L. M. Rasmijn, G. van der Schrier, R. Bintanja, J. Barkmeijer, A. Sterl, and W. Hazeleger, "Future equivalent of 2010 Russian heatwave intensified by weakening soil moisture constraints," *Nature Climate Change*, vol. 8, pp. 381–385, 2018.
[5] M. Kachi *et al.*, *Status of GCOM-W1/AMSR2 Development and Science Activities*, vol. 7106. Bellingham WA, USA: SPIE, 2008.
[6] E. G. Njoku, T. J. Jackson, V. Lakshmi, T. K. Chan, and S. V. Nghiem, "Soil moisture retrieval from AMSR-E," *IEEE Trans. Geosci. Remote Sens.*, vol. 41, no. 2, pp. 215–229, Feb. 2003.
[7] Y. H. Kerr *et al.*, "The SMOS mission: New tool for monitoring key elements of the global water cycle," in *Proc. IEEE*, vol. 98, no. 5, pp. 666–687, May 2010.
[8] D. Entekhabi *et al.*, "The soil moisture active passive (SMAP) mission," in *Proc. IEEE*, vol. 98, no. 5, pp. 704–716, May 2010.

[9] T. J. Jackson, "III. Measuring surface soil moisture using passive microwave remote sensing," *Hydrol. Processes*, vol. 7, pp. 139–152, 1993.

[10] J. Wigneron *et al.*, "L-band microwave emission of the biosphere (L-MEB) model: Description and calibration against experimental data sets over crop fields," *Remote Sens. Environ.*, vol. 107, pp. 639–655, 2007.

[11] Y. Kerr *et al.*, "The SMOS soil moisture retrieval algorithm," *IEEE Trans. Geosci. Remote Sens.*, vol. 50, no. 5, pp. 1384–1403, May 2012.

[12] B. Team, "SMOS-BEC land products description," *BEC-SMOS-0002-PD-Land.pdf, Version 1.0*, 2018.

[13] H. Fujii, T. Koike, and K. Imaoka, "Improvement of the AMSR-E algorithm for soil moisture estimation by introducing a fractional vegetation coverage dataset derived from MODIS data," *J. Remote Sens.*, vol. 29, pp. 282–292, 2009.

[14] T. Koike *et al.*, "Development of an advanced microwave scanning radiometer (AMSR-E) algorithm for soil moisture and vegetation water content," *Doboku Gakkai Ronbunshuu B*, vol. 48, pp. 217–222, 2004.

[15] M. Owe, R. De Jeu, and T. R. H. Holmes, "Multisensor historical climatology of satellite-derived global land surface moisture," *J. Geophys. Res.*, vol. 113, 2008, Art. no. F1.

[16] M. Parrens, "Considering combined or separated roughness and vegetation effects in soil moisture retrievals," *Int. J. Appl. Earth Observ. Geoinf.*, vol. 55, pp. 73–86, 2017.

[17] R. Fernandezmoran *et al.*, "A new calibration of the effective scattering albedo and soil roughness parameters in the SMOS SM retrieval algorithm," *Int. J. Appl. Earth Observ. Geoinf.*, vol. 62, pp. 27–38, 2017.

[18] J. Wigneron *et al.*, "Modelling the passive microwave signature from land surfaces: A review of recent results and application to the L-band SMOS & SMAP soil moisture retrieval algorithms," *Remote Sens. Environ.*, vol. 192, pp. 238–262, 2017.

[19] J.-P. Wigneron *et al.*, "SMOS-IC data record of soil moisture and L-VOD: Historical development, applications and perspectives," *Remote Sens. Environ.*, vol. 254, 2021, Art. no. 112238.

[20] A. Al-Yaari *et al.*, "Assessment and inter-comparison of recently developed/reprocessed microwave satellite soil moisture products using ISMN ground-based measurements," *Remote Sens. Environ.*, vol. 224, pp. 289–303, 2019.

[21] H. Ma, J. Zeng, N. Chen, X. Zhang, M. H. Cosh, and W. Wang, "Satellite surface soil moisture from SMAP, SMOS, AMSR2 and ESA CCI: A comprehensive assessment using global ground-based observations," *Remote Sens. Environ.*, vol. 231, 2019, Art. no. 111215.

[22] M. S. Yee, J. P. Walker, C. Rüdiger, R. M. Parinussa, T. Koike, and Y. H. Kerr, "A comparison of SMOS and AMSR2 soil moisture using representative sites of the oznet monitoring network," *Remote Sens. Environ.*, vol. 195, pp. 297–312, 2017.

[23] A. Colliander *et al.*, "Validation of SMAP surface soil moisture products with core validation sites," *Remote Sens. Environ.*, vol. 191, pp. 215–231, 2017.

[24] H. Kim *et al.*, "Global scale error assessments of soil moisture estimates from microwave-based active and passive satellites and land surface models over forest and mixed irrigated/dryland agriculture regions," *Remote Sens. Environ.*, vol. 251, 2020, Art. no. 112052.

[25] J. Zeng, Z. Li, Q. Chen, H. Bi, J. Qiu, and P. Zou, "Evaluation of remotely sensed and reanalysis soil moisture products over the Tibetan Plateau using in-situ observations," *Remote Sens. Environ.*, vol. 163, pp. 91–110, 2015.

[26] Y. Chen *et al.*, "Evaluation of SMAP, SMOS, and AMSR2 soil moisture retrievals against observations from two networks on the Tibetan Plateau," *J. Geophys. Res.: Atmos.*, vol. 122, pp. 5780–5792, 2017.

[27] J. Liu *et al.*, "Evaluation of SMAP, SMOS-IC, FY3B, JAXA, and LPRM soil moisture products over the Qinghai-Tibet plateau and its surrounding areas," *Remote Sens.*, vol. 11, pp. 792–792, 2019.

[28] Z. Su *et al.*, "The Tibetan Plateau observatory of plateau scale soil moisture and soil temperature (Tibet-Obs) for quantifying uncertainties in coarse resolution satellite and model products," *Hydrol. Earth Syst. Sci.*, vol. 15, pp. 2303–2316, 2011.

[29] K. Yang, "A multi-scale soil moisture and freeze-thaw monitoring network on the Tibetan Plateau and its applications," *Bull. Amer. Meteorol. Soc.*, vol. 94, pp. 1907–1916, 2013.

[30] X. Li *et al.*, "Hydrological cycle in the Heihe River Basin and its implication for water resource management in endorheic basins," *J. Geophys. Res.-Atmos.*, vol. 123, pp. 890–914, Jan. 2018.

[31] T. Zhao *et al.*, "Soil moisture experiment in the Luan River supporting new satellite mission opportunities," *Remote Sens. Environ.*, vol. 240, 2020, Art. no. 111680.

[32] H. Cui *et al.*, "Evaluation and analysis of AMSR-2, SMOS, and SMAP soil moisture products in the Genhe area of China," *J. Geophys. Res.*, vol. 122, pp. 8650–8666, 2017.

[33] X. Li *et al.*, "Heihe watershed allied telemetry experimental research (HiWATER): Scientific objectives and experimental design," *Bull. Amer. Meteorol. Soc.*, vol. 94, pp. 1145–1160, Aug. 2013.

[34] R. Jin *et al.*, "A nested ecohydrological wireless sensor network for capturing the surface heterogeneity in the midstream areas of the Heihe River Basin, China," *IEEE Geosci. Remote Sens. Lett.*, vol. 11, no. 11, pp. 2015–2019, Nov. 2014.

[35] J. I. N. Rui and K. Jian, "Hourly soil moisture dataset observed by eco-hydrological sensor network in the upper reaches of Heihe river (2013–2017)," National Tibetan Plateau Data Center, 2021.

[36] S. Liu *et al.*, "The Heihe integrated observatory network: A basin-scale land surface processes observatory in China," *Vadose Zone J.*, vol. 17, 2018, Art. no. 180072.

[37] Y. Aixia, "HiWATER: Land cover map of the Heihe river basin," National Tibetan Plateau Data Center, 2016.

[38] P. O'Neill, S. Chan, E. Njoku, T. Jackson, and R. Bindlish, *Soil Moisture Active Passive (SMAP) Algorithm Theoretical Basis Document Level 2 & 3 Soil Moisture (Passive) Data Products*. Pasadena, CA, USA: Jet Propulsion Laboratory, NASA, 2015.

[39] P. Miriam, M. José, P. María, S. Nilda, V. Mercè, and C. Adriano, "Multi-temporal evaluation of soil moisture and land surface temperature dynamics using in situ and satellite observations," *Remote Sens.*, vol. 8, 2016, Art. no. 587.

[40] A. A. Bitar *et al.*, "The global SMOS level 3 daily soil moisture and brightness temperature maps," *Earth Syst. Sci. Data*, vol. 9, pp. 293–315, 2017.

[41] X. Li *et al.*, "Compared performances of SMOS-IC soil moisture and vegetation optical depth retrievals based on Tau-Omega and Two-Stream microwave emission models," *Remote Sens. Environ.*, vol. 236, 2019, Art. no. 111502.

[42] T. R. H. Holmes, R. A. M. De Jeu, M. Owe, and A. J. Dolman, "Land surface temperature from Ka-band (37 GHZ) passive microwave observations," *J. Geophys. Res.*, vol. 114, 2009, Art. no. D4.

[43] A. G. C. A. Meesters, R. A. M. De Jeu, and M. Owe, "Analytical derivation of the vegetation optical depth from the microwave polarization difference index," *IEEE Geosci. Remote Sens. Lett.*, vol. 2, no. 2, pp. 121–123, Feb. 2005.

[44] Y. H. Kerr *et al.*, "Overview of SMOS performance in terms of global soil moisture monitoring after six years in operation," *Remote Sens. Environ.*, vol. 180, pp. 40–63, 2016.

[45] A. Alyaari *et al.*, "Assessment and inter-comparison of recently developed/reprocessed microwave satellite soil moisture products using ISMN ground-based measurements," *Remote Sens. Environ.*, vol. 224, pp. 289–303, 2019.

[46] S. K. Chan *et al.*, "Assessment of the SMAP passive soil moisture product," *IEEE Trans. Geosci. Remote Sens.*, vol. 54, no. 8, pp. 4994–5007, Aug. 2016.

[47] H. Cui, L. Jiang, J. Du, S. Zhao, and J. Wang, "Evaluation and analysis of AMSR-2, SMOS, and SMAP soil moisture products in the Genhe area of China," *J. Geophys. Res.: Atmos.*, vol. 122, pp. 8650–8666, 2017.

[48] T. Zhao *et al.*, "Soil moisture retrievals using L-band radiometry from variable angular ground-based and airborne observations," *Remote Sens. Environ.*, vol. 248, 2020, Art. no. 111958.

[49] Z. Wang, T. Che, and Y. Liou, "Global sensitivity analysis of the L-MEB model for retrieving soil moisture," *IEEE Trans. Geosci. Remote Sens.*, vol. 54, no. 5, pp. 2949–2962, May 2016.

[50] D. Zheng *et al.*, "Impact of surface roughness, vegetation opacity and soil permittivity on L-band microwave emission and soil moisture retrieval in the third pole environment," *Remote Sens. Environ.*, vol. 209, pp. 633–647, 2018.

[51] J. P. Grant *et al.*, "Comparison of SMOS and AMSR-E vegetation optical depth to four MODIS-based vegetation indices," *Remote Sens. Environ.*, vol. 172, pp. 87–100, 2016.

[52] M. Wang *et al.*, "An alternative AMSR2 vegetation optical depth for monitoring vegetation at large scales," *Remote Sens. Environ.*, vol. 263, 2021, Art. no. 112556.

[53] B. J. Choudhury *et al.*, "A parameterization of effective soil temperature for microwave emission," *J. Geophys. Res.*, vol. 87, pp. 1301–1304, 1982.

[54] D. Zheng *et al.*, "Sampling depth of L-band radiometer measurements of soil moisture and freeze-thaw dynamics on the Tibetan Plateau," *Remote Sens. Environ.*, vol. 226, pp. 16–25, 2019.

Zengyan Wang received the B.S. and Ph.D. degrees in cartography and geographic information system from the University of Chinese Academy of Sciences, Beijing, China, in 2012 and 2017, respectively, fostered by the Northwest Institute of Eco-Environment and Resources (originally the Cold and Arid Regions Environmental and Engineering Research Institute, CAREERI), Chinese Academy of Sciences, Lanzhou, China.

She is currently a Lecturer with the College of Geography and Environmental Science, Henan University, Kaifeng, China. She is also a Member of the Key Laboratory of Geospatial Technology for the Middle and Lower Yellow River Regions (Henan University), the Ministry of Education. Her research interests include retrieval, validation, and applications of remotely sensed soil moisture from combined optical and microwave observations, and related scaling issues.

Liyun Dai received the B.S. degree in geography from the Lanzhou University, Lanzhou, China, in 2004, and the Ph.D. degree in cartography and geographic information system from the Cold and Arid Regions and Environmental and Engineering Institute (CAREERI), Chinese Academy of Science (CAS), Beijing, China, in 2013.

From 2014 to 2017, she was an Assistant Professor in remote sensing of snow with the CAREERI. Since 2018, she has been an Associate Professor with the Northwest Institute of Eco-Environment and Resources, CAS. Her research interests include observation of snow parameters, evolution in snow parameters, simulation of snow parameters, and estimation of snow parameters using remote sensing technique.

Tao Che (Member, IEEE) received the Ph.D. degree in cartography and geographic information system from the Cold and Arid Regions Environmental and Engineering Research Institute, Chinese Academy of Sciences (CAS), Lanzhou, China, in 2006.

Since 2014, he has been a Professor with the Northwest Institute of Eco-Environment and Resources, CAS, Lanzhou, China. He is currently the Head of the laboratory of Remote Sensing and Geographic Information Sciences in the Northwest Institute of Eco-Environment and Resources, as well as the head of the Heihe Remote Sensing Experimental Research Station of CAS. His research interests include the remote sensing of land surface parameters in cold and arid regions, and snow water equivalent retrieval with microwave remote sensing.

Xiaojun Li received the M.S. degree in electronics and communication engineering from the University of Chinese Academy of Sciences, Beijing, China, in 2018. He is currently working toward the Ph.D. degree sponsored by China Scholarship Council (201804910838) in "Improvement of the SMOS-IC retrievals of soil moisture and vegetation L-VOD index" at the INRAE, Bordeaux, France.

He developed the SMOS-IC version 2 (V2) retrieval product and is currently responsible for the evaluation and release of the SMOS-IC V2 products. His research interests include microwave soil moisture retrieval models, validation, and carbon cycle estimation.
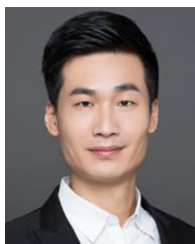
Tianjie Zhao (Senior Member, IEEE) received the B.S. and Ph.D. degrees in cartography and geographic information systems from Beijing Normal University, Beijing, China, in 2007 and 2012, respectively.

From 2010 to 2012, he was a Visiting Scientist with the Hydrology and Remote Sensing Laboratory, Agricultural Research Service, U.S. Department of Agriculture, Beltsville, MD, USA. He is currently an Associate Professor with the State Key Laboratory of Remote Sensing Science, Aerospace Information Research Institute, Chinese Academy of Sciences, Beijing, China, and he is a member of the Youth Innovation Promotion Association Program. His research interests include microwave radiometry of soil moisture and its freeze-thaw process.

Dr. Zhao was the recipient of the scholarship award for excellent doctoral student granted by the Ministry of Education of China in 2011, the Young Scientist Award from the International Union of Radio Science in 2014, and the Young Scientist Award from Progress in Electromagnetics Research Symposium in 2018.

Jean-Pierre Wigneron (Senior Member, IEEE) received the M.Sc. degree in engineering from the Ecole Nationale Supérieure de l'Aéronautique et de l'Espace, Toulouse, France, in 1987, and the Ph.D. degree in remote sensing, climate and ecology from the University of Toulouse, Toulouse, France, in 1993.

He is currently a Senior Research Scientist with the Interactions Sol Plante Atmosphere, INRAE Bordeaux, Bordeaux, France, the Head of the remote sensing group. He developed pioneer work in 2-parameter retrievals of soil moisture & biomass from inversion of the L-band Microwave Emission of the Biosphere model. He is a PI of SMOS-IC, an alternative SMOS product of soil moisture and L-VOD (https://ib.remote-sensing.inrae.fr); SMOS-IC does not use ancillary data and is robust in monitoring the water and carbon cycles in the tropical, temperate, and boreal regions. Improved VOD indices are now developed from Sentinel-1, ASCAT, AMSR2, and SMAP. He has authored or coauthored more than 200 papers in international peer-reviewed journals. His research interests include microwave remote sensing of soil and vegetation, radiative transfer, water and carbon cycle in forests.

Dr. Wigneron has been an Associate Editor of Remote Sensing of Environment, since 2014.